


Article

Enhancement Study of the Photoactivity of TiO₂ Photocatalysts during the Increase of the WO₃ Ratio in the Presence of Ag Metal

Sharah H. Aldirham ^{1,*}, Ahmed Helal ², Mohd Shkir ¹ , M. A. Sayed ¹ and Atif Mossad Ali ^{1,*}

¹ Department of Physics, Faculty of Science, King Khalid University, Abha 61413, Saudi Arabia; shkirphysics@kku.edu.sa (M.S.); masyeed@kku.edu.sa (M.A.S.)

² Nanostructured Materials and Nanotechnology Department, Advanced Materials Institute, Central Metallurgical R&D Institute (CMRDI), P.O. Box 87 Helwan, Cairo 11421, Egypt; ahmed_helal@cmrdi.sci.eg

* Correspondence: saldrhm@kku.edu.sa (S.H.A.); atifali@kku.edu.sa (A.M.A.)

Abstract: Nanocomposites (NCs) consisting of 4%Ag/*x*%WO₃/TiO₂, with varied concentrations (*x* = 1, 3, 5, 7 wt.%) of WO₃, were successfully synthesized using the sol-gel process to examine their photocatalytic performance. The synthesized 4%Ag/*x*%WO₃/TiO₂ nanopowder was characterized using X-ray diffraction (XRD), Raman spectroscopy, scanning electron microscopy (SEM), transmission electron microscopy (TEM), UV–vis diffuse reflectance spectra (UV–vis DRS), photoluminescence (PL), and Brunauer–Emmett–Teller (BET) surface area analysis to elucidate its physicochemical properties. The photocatalytic evaluation revealed that the Ag/1%WO₃/TiO₂ nanocomposite exhibits 98% photoreduction efficiency for Cr(VI) after 2 h under visible light due to the impact of the plasmonic effect of Ag atoms. In addition, the Ag/4%WO₃/TiO₂ shows about 95% photooxidation efficiency for methylene blue (MB) dye after 4 h.

Keywords: Ag/WO₃/TiO₂; plasmon effect; photocatalysis; Cr(VI) reduction; methylene blue



Citation: Aldirham, S.H.; Helal, A.; Shkir, M.; Sayed, M.A.; Ali, A.M. Enhancement Study of the Photoactivity of TiO₂ Photocatalysts during the Increase of the WO₃ Ratio in the Presence of Ag Metal. *Catalysts* **2024**, *14*, 633. <https://doi.org/10.3390/catal14090633>

Academic Editor: Natalia Martinsovich

Received: 22 July 2024

Revised: 9 September 2024

Accepted: 11 September 2024

Published: 18 September 2024



Copyright: © 2024 by the authors. Licensee MDPI, Basel, Switzerland. This article is an open access article distributed under the terms and conditions of the Creative Commons Attribution (CC BY) license (<https://creativecommons.org/licenses/by/4.0/>).

1. Introduction

Titanium dioxide (TiO₂) is renowned as a highly promising photocatalyst due to its advantages, such as its photostability, low cost, and non-toxicity [1,2]. However, its photocatalytic activity is limited to ultraviolet (UV) light due to its wide bandgap (3.20 eV), which constitutes only 3–5% of the total solar irradiance [3]. To address this, researchers have explored modifications like metal doping composites with other materials to shift its optical response into the visible range [4]. One effective approach involves doping TiO₂ with metals (e.g., Ag, Au, and Cr) and rare earth metals (Eu, Ce etc.) [5,6], or nonmetal atoms (e.g., N, S, and F). These modifications can trap electrons, enhance charge separation, and decrease the bandgap, potentially leading to new sunlight-driven photocatalysts [7–10]. Additionally, coupling TiO₂ with other semiconductors (such as SnO₂, and WO₃) can extend the photoexcitation energy range that improves pollutant photodegradation [11]. Fundamentally, WO₃ possesses a conduction band potential of +0.77 eV [12], enabling a new band position that efficiently receives photogenerated electrons from the conduction band of TiO₂. Therefore, introducing tungsten doping into TiO₂ matrices has resulted in higher electrical conductivity [13]. The exploration of TiO₂/WO₃ composites has emerged as a prominent area of research, driven by their promising properties and diverse functionalities. For instance, TiO₂-supported WO₃ has demonstrated remarkable efficacy as a heterogeneous catalyst for redox reactions [14]. Additionally, synthesizing highly ordered cubic mesoporous WO₃/TiO₂ thin films has enhanced photocatalytic activity compared to pure TiO₂ films [15]. Furthermore, studies by Reyes-Gil et al. (2013) and Reyes-Gil et al. (2015) highlighted the enhanced ion storage capacity and electrochromic activity of WO₃/TiO₂ nanostructures, underscoring the significance of composite materials in

advanced applications [16,17]. Archana et al. (2014) also investigated the photocatalytic and electrical properties of WO₃-doped TiO₂ nanowires, revealing promising results for high-efficiency dye-sensitized solar cells [13]. These recent literature reviews provide valuable insights into the multifaceted properties of nanocomposites, offering a comprehensive understanding of their structural, optical, electrical, dielectric, and photocatalytic characteristics and paving the way for further advancements in diverse technological applications. Despite these advancements, challenges persist, particularly in supercapacitors and photocatalysis utilizing TiO₂-based materials. [18,19]. Additionally, TiO₂-based photocatalysts often suffer from relatively low photocatalytic efficiency and limited light absorption in the visible region [20], which restricts their practical applications. To address these challenges, incorporating Ag nanoparticles and WO₃ into TiO₂-based materials may offer promising solutions. Ag nanoparticles possess excellent electrical conductivity, which can enhance the charge transport within TiO₂ matrices. Li et al. prepared Ag/WO₃/TiO₂ nanowires via the hydrothermal technique [21]. They reported that the as-prepared composite photocatalysts showed greatly improved absorbance even in the infrared regime and dramatically improved photocatalytic activities toward methyl orange degradation in comparison to those of pure TiO₂ nanowires. In addition, the as-prepared Ag/WO₃/TiO₂ composite exhibited excellent recyclability for pollutant degradation. It is suggested that, with the synergetic help of WO₃ and Ag nanoparticles, more photogenerated electrons and hole pairs can be produced, participate in the photodegradation reaction, and enhance the photocatalytic activity dramatically [22]. Xu et al. used an aqueous sol-gel route for the preparation of nanostructured Ag-WO₃/TiO₂ [23]. Ag-WO₃/TiO₂ nanoparticles with a mixed phase (anatase/rutile) showed more excellent photocatalytic activity on the removal of MB than single-doped TiO₂, owing to their small particle size distribution, larger surface area, and higher absorbance of visible light [23]. Ag@TiO₂/WO₃ was synthesized using the sol-gel method and its photocatalytic activity was enhanced compared to its counterparts [24]. The rate of degradation of methylene blue (MB) using Ag@TiO₂/WO₃ was ~20 and ~25 times higher in contrast with pure TiO₂ and Degussa P25, respectively. This increase in the photocatalytic performance was because of the enhancement of light harvesting, a large amount of charge carrier injection due to the surface plasmon resonance effect exhibited by Ag nanoparticles under the irradiation of visible light, and a lower recombination rate due to the ease of charge carrier transfer through the junction between the two metal oxides [24]. Similarly, the addition of WO₃ to TiO₂ matrices can significantly enhance photocatalytic performance. WO₃ possesses a favorable electronic band structure and a high surface area, facilitating the charge transfer processes [25]. In photocatalysis, WO₃ acts as a co-catalyst, promoting the separation of photoinduced charge carriers and enhancing photocatalytic activity, particularly in the visible light region [26]. In this paper, we aim to see the impact of the variation of the %WO₃ weight ratio with 4% Ag doping on structural, optical, and photocatalytic properties of TiO₂ NPs. The pure and doped TiO₂ NPs were prepared using the facile sol-gel method and studied from the application point of view. The obtained results are discussed in different sections of the article. The composite revealed that the photoactivity was enhanced, which was clear from the photoreduction of Cr(VI) ions and photodegradation of MB dye.

2. Result and Discussion

The X-ray diffraction (XRD) technique confirmed the phase structure of the prepared nanocomposite samples. XRD patterns for pure TiO₂ and 4% Ag/*x*%WO₃/TiO₂ (*x* = 1, 3, 5, and 7%) nanocomposites are represented in Figure 1a. They revealed that all samples are related to the classic anatase structure of TiO₂, showing patterns at $2\theta = 25.6^\circ, 37.8^\circ, 48.18^\circ, 54.1^\circ, 55.2^\circ, 62.8^\circ, 69^\circ, \text{ and } 70.5^\circ$, which are related to the (101), (004), (200), (105), (211), (204), (116), and (220) planes, respectively, and are matched to the standard card of TiO₂ [JCPDS#21-1272] [27,28]. The face-centered cubic metallic Ag crystal structure is associated with the diffraction peaks (200) and (220) at 44.48° and 64.68° (JCPDS# 87-0597), respectively. Incorporating various weight percentages of 1, 3, 5, and 7 wt.% of WO₃

onto 4% Ag/TiO₂ leads to the appearance of the diffraction peaks of WO₃ for 5% and 7% between $2\theta = 23.5^\circ$ and 25° for the (002), (020), and (200) planes. The slight shift in the characteristic peaks of TiO₂ at $2\theta = 25.4^\circ$, shown in Figure 1b, could be attributed to the shrinking of the crystallite size due to the replacement of the Ti atom by the W atom. The W⁶⁺ ion can easily replace the Ti⁴⁺ ion in the TiO₂ lattice because the radius of W⁶⁺ is 62 pm smaller than Ti⁴⁺ ions, which equals to 68 pm [29]. It is important to investigate the microstructural parameters of any material synthesized at the nanoscale and to see the impact of doping on such parameters. Hence, herein we have investigated the impact of doping on the crystallinity of TiO₂, and we have estimated the crystallite size (D) values of the prepared nanocomposites for the most intense peak (101) using the Scherrer equation:

$$D = \frac{k\lambda}{\beta \cos\theta} \quad (1)$$

where β denotes the full width at half maximum (FWHM), k is the shape factor with a value of 0.9, and λ represents the wavelength of the XRD source. The calculated D values of the prepared pure WO₃, pure TiO₂ NPs, and 4% Ag/ x %WO₃/TiO₂ (with $x = 1, 3, 5$, and 7 wt.% of WO₃) nanocomposites are presented in Table 1. The crystallite size values decrease systematically when the WO₃ dopant ratio increase in TiO₂. Also, the other parameters of the structure, such as the dislocation density (δ) and the microstrain (ϵ), were calculated using FWHM for the most intense peak (101) and its angular position for the prepared samples by [30,31]:

$$\delta = \frac{1}{D^2} \quad (2)$$

$$\epsilon = \frac{\beta}{4\tan\theta} \quad (3)$$

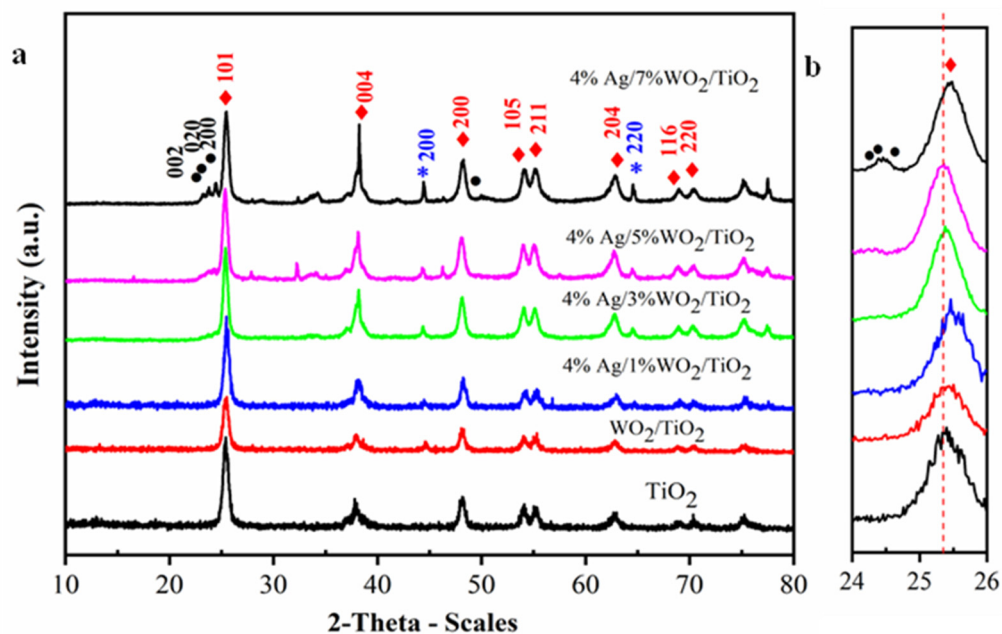


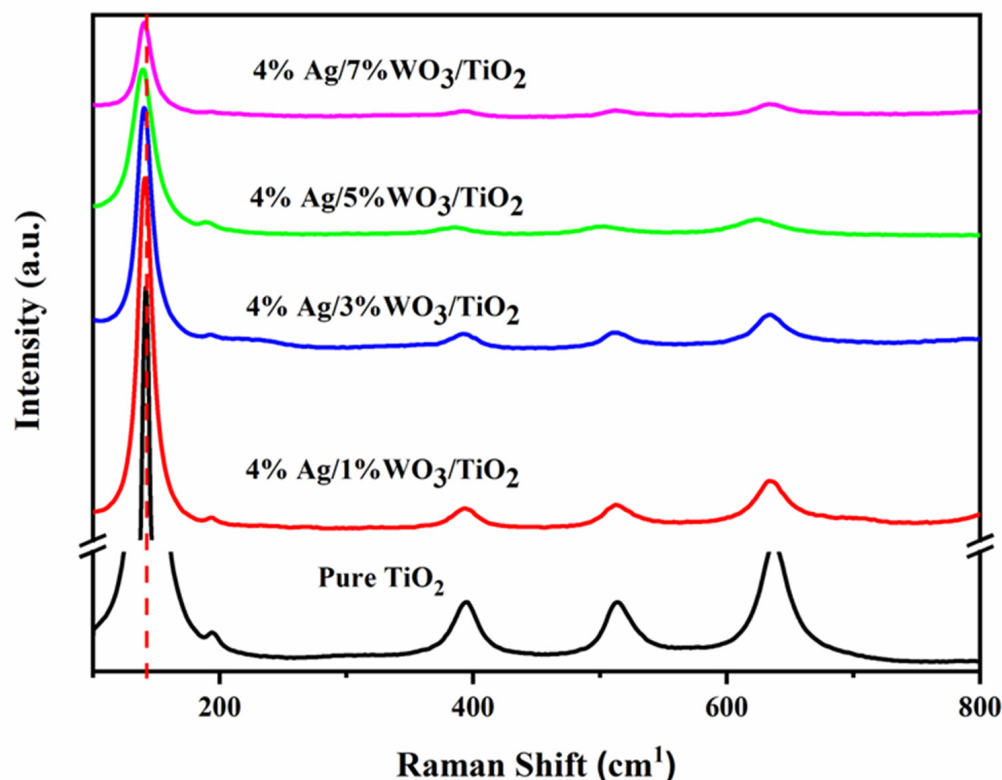
Figure 1. (a) The XRD patterns of the synthesized pure TiO₂ and 4% Ag/ x %WO₃/TiO₂ ($x = 1, 3, 5$, and 7%) nanocomposites; (b) magnification in rang 2θ (25–26).

Table 1. The estimated values of D, δ , and ϵ .

Sample	D (nm)	δ	ϵ
Pure TiO ₂	17.01	3.45×10^{-3}	9.27×10^{-3}
WO ₃ /TiO ₂	15.77	3.50×10^{-3}	9.14×10^{-3}
4%Ag/1%WO ₃ /TiO ₂	15.94	3.93×10^{-3}	9.90×10^{-3}
4%Ag/3%WO ₃ /TiO ₂	15.91	3.94×10^{-3}	9.89×10^{-3}
4%Ag/5%WO ₃ /TiO ₂	14.50	4.75×10^{-3}	10.8×10^{-3}
4%Ag/7%WO ₃ /TiO ₂	13.98	5.11×10^{-3}	11.2×10^{-3}

The estimated values of δ and ϵ are also presented in Table 1. The given values of δ after doping WO₃/TiO₂ with 4%Ag samples increase as the D values decrease. The δ values increase when increasing the WO₃ content, whereas the ϵ values vary between 11.2×10^{-3} and 7.55×10^{-3} . These microstructural parameters indicate the impact of doping.

To confirm the changes in the prepared samples, Raman spectra for pure TiO₂ and 4% Ag/ x %WO₃/TiO₂ (with $x = 1, 3, 5$, and 7 wt.% of WO₃) nanocomposites were recorded and are displayed in Figure 2.

**Figure 2.** Raman spectra of 1 pure TiO₂ and 4% Ag/ x %WO₃/TiO₂ ($x = 1, 3, 5$, and 7%) nanocomposites.

The Raman spectra confirm the data extracted from the XRD graph that prove the anatase phase structure of pure TiO₂ and 4% Ag/ x %WO₃-doped TiO₂ nanocomposites. The tetragonal anatase titania exhibits typical vibration modes, with the most active modes at 143, 196, and 637 cm^{−1} corresponding to the Eg (symmetric stretching vibration) band, 395 cm^{−1} related to the A1g (symmetric bending vibration) band, and 513 that corresponds to B1g (antisymmetric bending vibration) modes [32]. Moreover, there is a slight redshift to the lower wavenumber for the peak at 141 cm^{−1} with an increase in the WO₃ weight ratio due to the insertion of a small radius of W⁶⁺ that equals 62 pm into the TiO₂ molecule that has a radius of Ti⁴⁺ ions equal 68 pm according to the number of the available vacancies, causing shrinking of the unit cell [32–34].

High-resolution transmission electron microscopy (HRTEM) images were recorded to clarify the structural attributes of pure TiO_2 and $4\%\text{Ag}/x\%\text{WO}_3/\text{TiO}_2$ and nanocomposites (NCs), as shown in Figure 3.

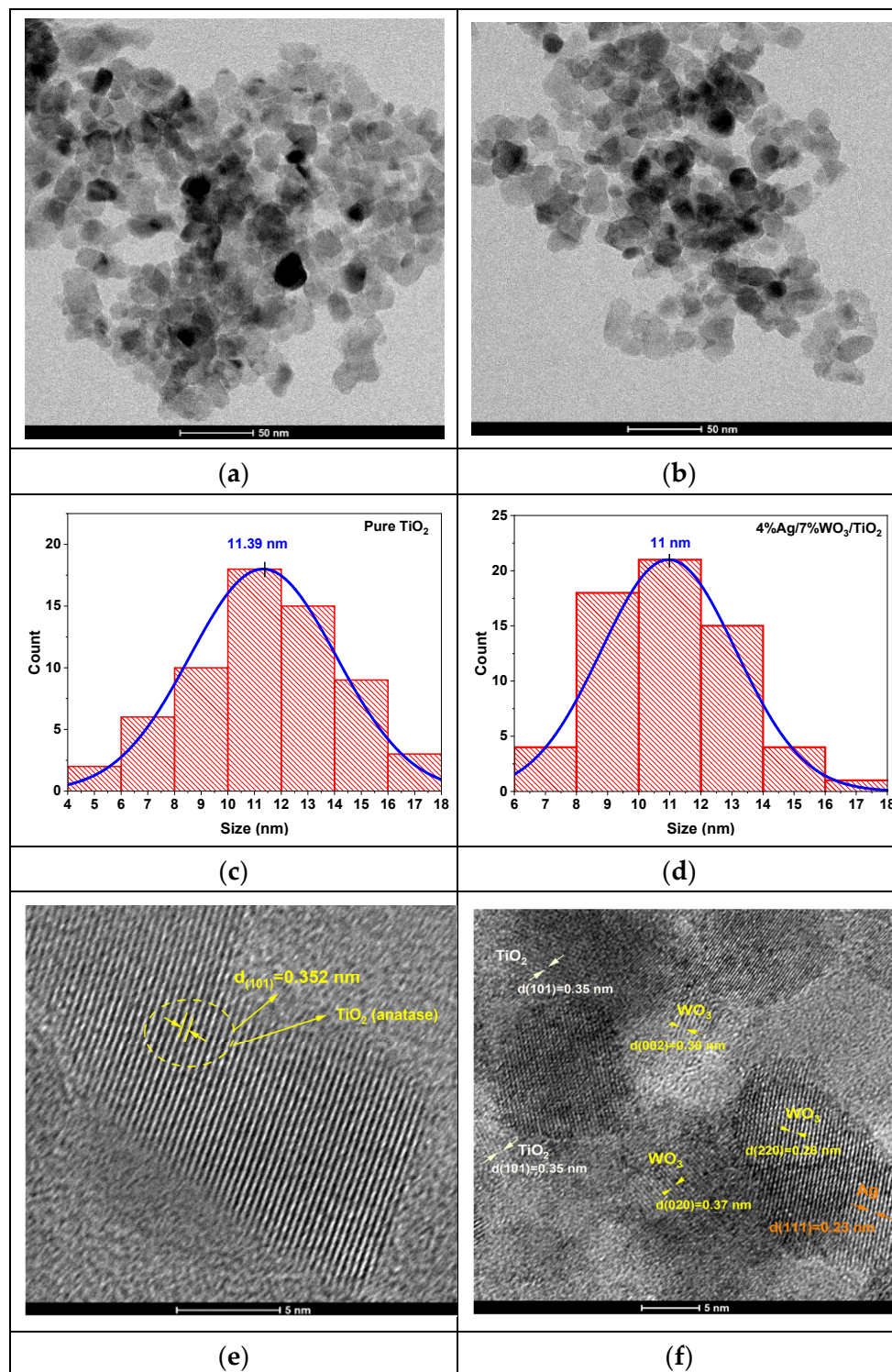


Figure 3. Cont.

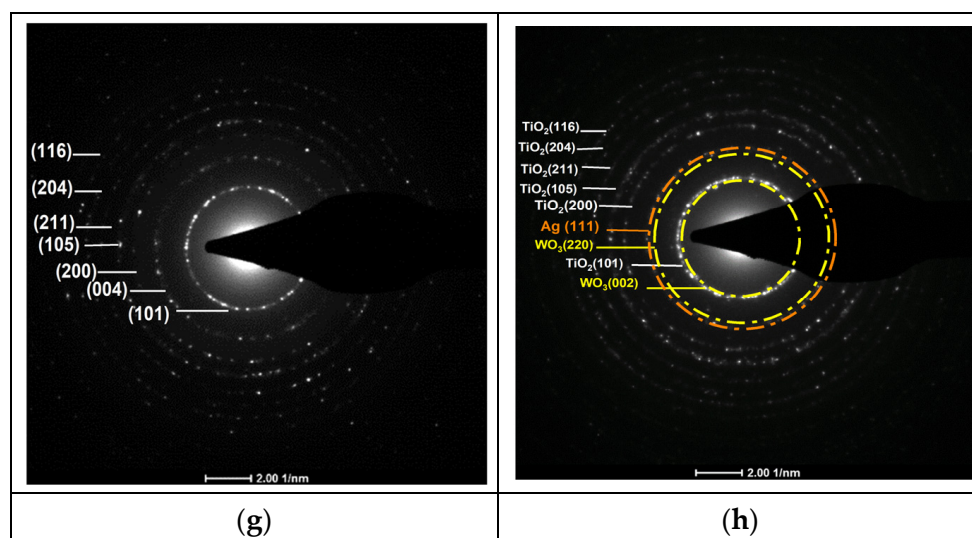


Figure 3. (a,b) TEM images of pure TiO₂ and 3%Ag/WO₃/TiO₂ nanocomposites; (c,d) particle size distributions; (e,f) HRTEM images of interplanar distances; (g,h) selected area electron diffraction (SAED).

Figure 3a,b prove that pure TiO₂ and 4%Ag/3%WO₃/TiO₂ exhibit a homogenous morphology, with a grain size within the approximate range of 10–15 nm. The average particle sizes for the pure TiO₂ and its composite have been determined from the histograms in Figure 3c,d, which show particle size distributions of 11 nm and 11.39 nm for TiO₂ and 4%Ag/3%WO₃/TiO₂, respectively. The HR images of the TiO₂ and the composite, which are shown in Figure 3e–h, expose the presence of fringes that were identified by SAED pattern lattice spacing values of 0.352 nm corresponding to the lattice spacing values of the (101) plane of anatase TiO₂, 0.38 nm that agrees with the (002) plane of monoclinic WO₃, and 0.23 nm for the (111) plane; these values are in agreement with the XRD results and previous reports [34–37].

Employing the N₂ adsorption–desorption method described by Brunauer, Emmett, and Teller (BET), the physical adsorption of the produced samples was determined. The adsorption–desorption isotherms in Figure 4a display a type IV isotherm with mesopores and H₂-type hysteresis loops, indicating that the processed samples are categorized as mesoporous materials [38–42]. The surface area and pore size distribution curves, obtained using the Barrett–Joyner–Halenda (BJH) method and shown Figure 4b, reveal that the pore size decreased with an increase in the WO₃ content (Table 2) due to the incorporation of WO₃ particles into the pore of the TiO₂. However, at a higher 4% Ag/7%WO₃/TiO₂ content, the surface area increases again due to the sediment of the small-size WO₃ particles on the surface of the TiO₂. To evaluate the enhancement of the optical response of the prepared materials, UV–visible diffuse reflectance spectroscopy (UV-DRS) was employed. Figure 5a shows the absorbance spectra for pure TiO₂ and 4% Ag/*x*%WO₃/TiO₂ (with *x* = 1, 3, 5, and 7 wt.%) nanocomposites.

Table 2. The estimated values of the bandgap, SA, PV and Pd.

	Bandgap (eV)	SA (m ² /g)	PV [cm ³ g ^{−1}]	Pd [nm]
Pure TiO ₂	3.2	66.21	0.2624	18.983
4%Ag/1%WO ₃ /TiO ₂	2.72	62.56	0.2604	15.854
4%Ag/3%WO ₃ /TiO ₂	2.40	48.98	0.0795	5.9162
4%Ag/5%WO ₃ /TiO ₂	2.69	59.93	0.1806	12.003
4%Ag/7%WO ₃ /TiO ₂	2.82	63.08	0.1852	11.475

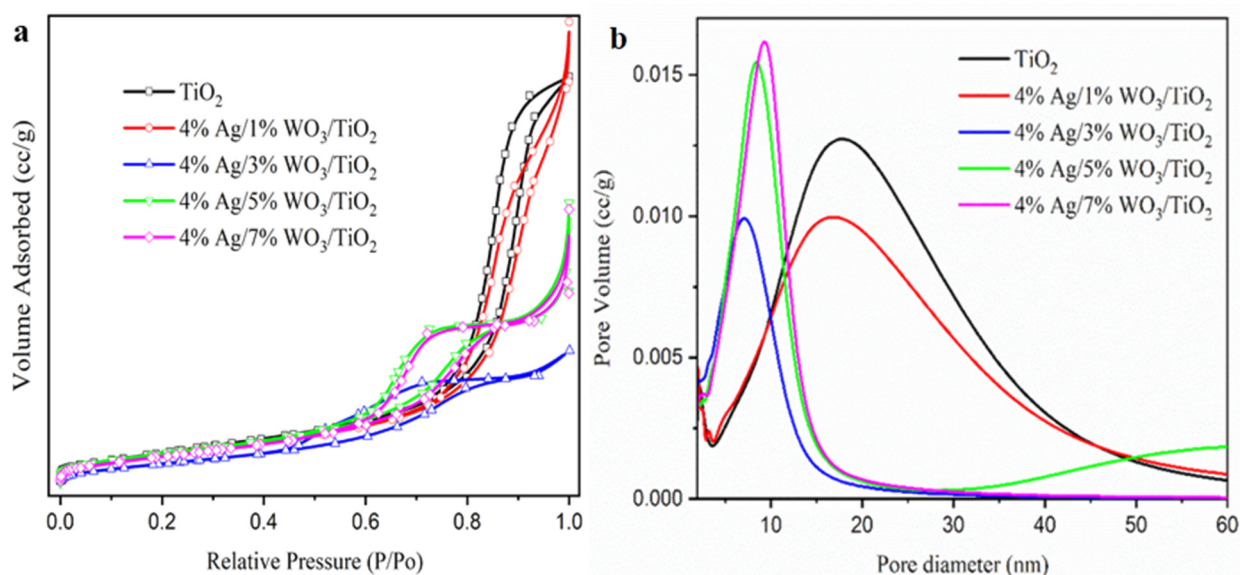


Figure 4. (a) The adsorption/desorption of BET isotherms, and (b) BJH of pure TiO₂ and 4% Ag/ x %WO₃/TiO₂ ($x = 1, 3, 5$, and 7%) nanocomposites.

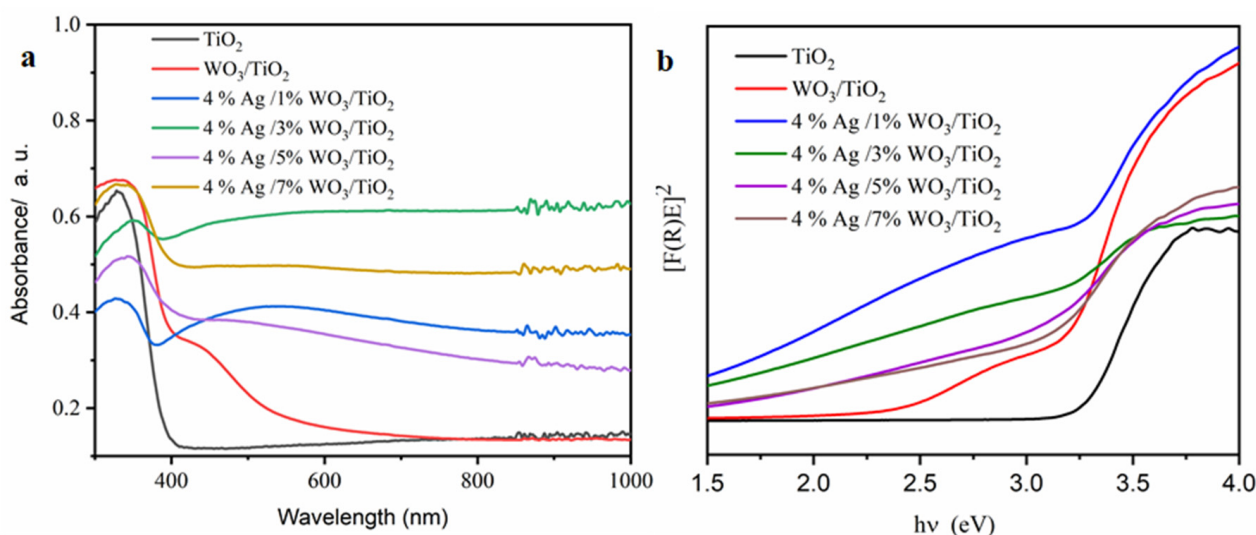


Figure 5. (a) The relationship among the absorbance and the wavelengths; (b) the relation among the direct $(F(R)E)^2$ nanocomposites' bandgap values with the photon energy ($h\nu$) for pure TiO₂ and 4% Ag/ x %WO₃/TiO₂ ($x = 1, 3, 5$, and 7%) nanocomposites.

The absorption edge of pure TiO₂ was observed at 380 nm, indicating that the sample has a high bandgap; however, for 4% Ag/3%WO₃/TiO₂ nanocomposites, the bandgap was noticed to be lowest viz. 2.40 eV due to the redshift in the absorption edge (Figure 5a). The Ag and WO₃ particles on the surface of the TiO₂ contribute to the composite's improvement [43].

The broad peaks ranged between 400 and 700 nm, especially in the 4% Ag/1%WO₃/TiO₂ sample (Figure 5a), due to plasmon-resonance Ag particles on the surface [24]. Furthermore, it was observed that with the increase in the WO₃ ratio, the plasmon peak decreased, and the absorption spectra around the heterojunction between WO₃/TiO₂ photocatalysts were wider and exhibited a redshift in comparison to the pristine titania [24]. The main source of this redshift is the lattice mismatch between the metal oxides, which leads to the formation of mid-gap states in the bandgap of titania.

The optical energy gap of the prepared samples was calculated using the Kubelka–Munk relation [44] as follows:

$$F(R) = \frac{(1 - R)^2}{2R} \quad (4)$$

where R is the reflectance. In terms of $F(R)$, Tauc's equation adjusts the result to become [45]:

$$F(R)h\nu = A(h\nu - E_g)^n \quad (5)$$

E_g refers to the bandgap as mentioned above, $h\nu$ represents the energy of light, $n = 1/2$ is for the direct allowed transition, and $n = 2$ is for the indirect allowed transition.

As shown in Figure 5b, the energy gap was reduced as a result of the WO_3 particles being loaded onto the TiO_2 surface, according to the data in Table 2. The increase in WO_3 concentration on the surface of the TiO_2 composite contributes to the decrease of the energy gap and, consequently, increases the conductivity of the prepared materials. PL was employed to investigate the impact of the increase in the WO_3 ratio on the charge carrier trapping and transfer into the prepared composites. The emission spectra of pure TiO_2 and 4% Ag/ $x\%WO_3/TiO_2$ (with $x = 1, 3, 5$, and 7 wt.% of WO_3) nanocomposites are displayed in Figure 6. The prepared samples were excited at 380 nm to obtain the emission spectra and the result exhibited two luminescence emissions at 450 nm and 470 nm; according to the results, the emission peak at 450 nm was related to the surface defects. The composite and the analysis of the effectiveness of the charge carrier trapping and transfer through the knowledge of the bath of e^-/h^+ pairs in semiconductors can be linked to particular electronic properties of the WO_3 – TiO_2 nanocomposites [46]. However, the recombination of excited charge carriers on the WO_3 surface is responsible for the emission peak at 467 nm [47]. The results reveal that the PL spectra were decreased with an increase in the WO_3 weight ratio at 4% Ag/ $x\%WO_3/TiO_2$ (with $x = 1, 3$ wt.% of WO_3) nanocomposites, which means that there is an increase in the lifetime of the electrons at the excited state that gives a high photonic efficiency and photocatalytic activity [48,49]. On the other hand, when the WO_3 weight ratio increases to 5 and 7%, the impurity energy level works as a charge carrier recombination center, and the PL spectrum re-increases again, which decreases the photonic efficiency and photocatalytic activity [30,50].

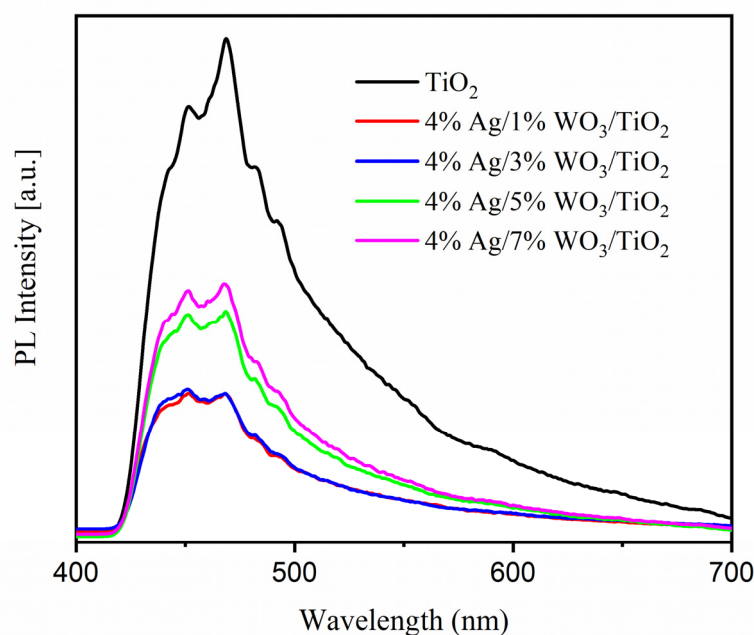


Figure 6. Photoluminescence spectra of pure TiO_2 and 4% Ag/ $x\%WO_3/TiO_2$ ($x = 1, 3, 5$, and 7%) nanocomposites.

The photocatalytic activity of pure TiO_2 , WO_3/TiO_2 , and with 4% Ag/ $x\%\text{WO}_3/\text{TiO}_2$ (with $x = 1, 3$ wt.% of WO_3) nanocomposites was studied using Cr(VI) as a heavy metal molecule photoreduction to nontoxic Cr(III). As presented in Figure 7a, the results demonstrate that the photoreduction efficiency of pure TiO_2 is 25%. Moreover, the photoreduction efficiency was nearly 95% in the 4% Ag/1% WO_3/TiO_2 sample. Nonetheless, the photoactivity was decreased after an increase of the 4% Ag/3% WO_3/TiO_2 to 78%, and re-increased again with 4% Ag/5% WO_3/TiO_2 , reaching 95% in the presence of 4% Ag/7% WO_3/TiO_2 . The obtained results are comparable with several previous reports [21,22,51–56] as provided in a comparative Table S1 (see supporting data). These changes are due to the two mechanisms' impact on the catalyst activity. First, the pure TiO_2 activity is very small due to the wide bandgap of the TiO_2 . The high activity of the 4% Ag/1% WO_3/TiO_2 sample is due to the impact of the plasmonic effect of the Ag metal that appeared clearly in the absorption graph. At the same time, the impact of the heterojunction between the TiO_2 and WO_3 molecules is very low. When the WO_3 molecule was increased to 3% and 5%, the impact of the plasmon effect was decreased. By contrast, the impact of the heterojunction between the TiO_2 and WO_3 molecules was increased till it reached 95% efficiency in the presence of the 4% Ag/7% WO_3/TiO_2 sample. Based on the pseudo-first-order model, the kinetics of Cr(VI) photoreduction over the synthesized photocatalysts were further explored as depicted in Figure 7b (Equation (6)) [21]:

$$\ln\left(\frac{C_0}{C_t}\right) = -k.t \quad (6)$$

where C_0 and C_t are the Cr(VI) concentration at time zero and time t , and k is the rate constant. By fitting the $\ln(C_t/C_0)$ vs. t curves, the 4% Ag/1% WO_3/TiO_2 and 4% Ag/7% WO_3/TiO_2 nanocomposite appear to have a k value almost nine times greater than that of pure TiO_2 , revealing that the Ag/ WO_3/TiO_2 nanocomposite serves as an outstanding and efficient photocatalyst for the Cr(VI) photoreduction.

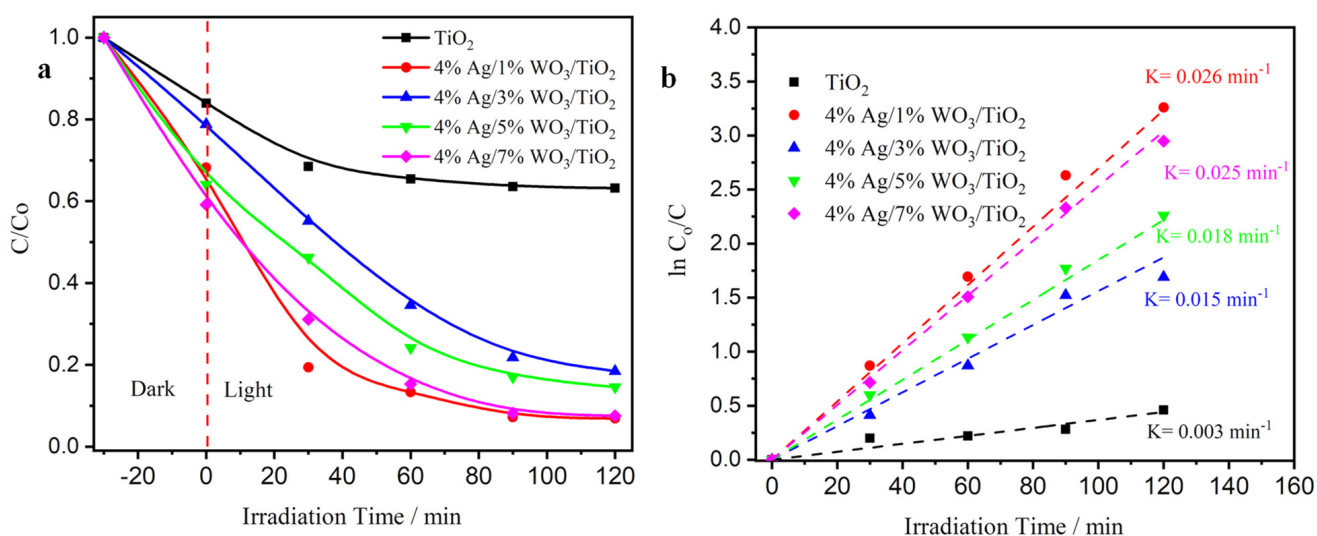


Figure 7. (a) Degradation curves of Cr(VI) solution; (b) plots of $\ln(C_0/C)$ versus irradiation time of pure TiO_2 and 4% Ag/ $x\%\text{WO}_3/\text{TiO}_2$ ($x = 1, 3, 5$, and 7%) nanocomposites.

The other technique is to evaluate the organic waste degradation activity of the prepared photocatalysts using a photooxidation mechanism. Figure 8a shows the photodegradation efficiency of MB dye discharged into waterways from the textile industrial sector. The results exhibit that the 4% Ag/5% WO_3/TiO_2 catalyst shows improved degradation efficiency of MB to 85% after 30 min and 93% after 4 h. the efficiency of the sample refers to the impact of the heterojunction between the TiO_2 and WO_3 , in addition to the

impact of the plasmon effect of Ag that works as a trapping point for the photogenerated electron and holes [23]. Figure 8b shows the photodegradation rates of MB that exposed the photodegradation following the first-order kinetics. The optimum sample showed a photodegradation rate nine times higher than that of the pure TiO_2 sample.

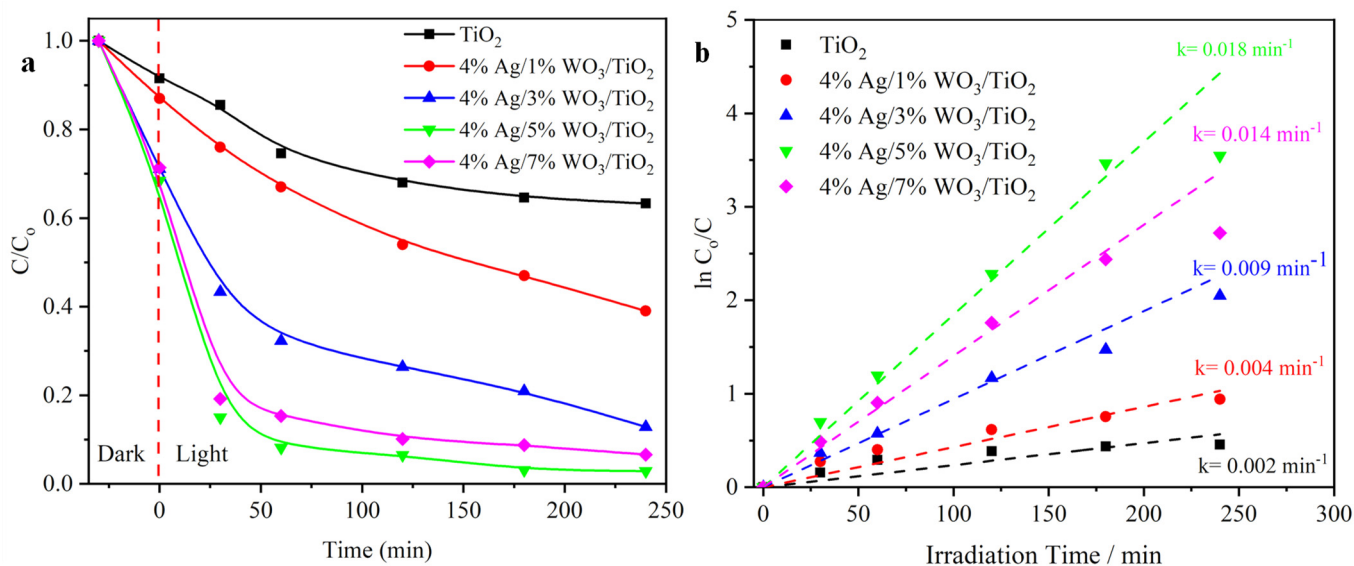


Figure 8. (a) Degradation curves of MB dye solution; (b) plots of $\ln(C_0/C)$ versus irradiation time of pure TiO_2 and 4% Ag/ $x\%\text{WO}_3/\text{TiO}_2$ ($x = 1, 3, 5$, and 7%) nanocomposites.

3. Materials and Methods

3.1. Materials

Titanium (IV) isopropoxide (97%) was sourced from Alfa Aesar, Ward Hill, Massachusetts, U.S., and tungsten (VI) chloride (99.9%), Pluronic P123 (a poly (ethylene glycol)-poly(propylene glycol) copolymer with a molecular weight of approximately 5800), hydrochloric acid, ammonium hydroxide (NH_4OH) with a purity of >98%, and silver nitrate (AgNO_3) were procured from Sigma-Aldrich, Burlington, Massachusetts, United States.

3.2. Methods

3.2.1. Synthesis of Titanium Nanoparticle TiO_2 (NPs)

TiO_2 nanoparticles were synthesized using the sol-gel method. The procedure involved the following steps. First, 23.4 mL of titanium isopropoxide was mixed with 9.38 mL of hydrochloric acid (HCl) under stirring for 10 min, resulting in a clear solution. After that, 5 g of Pluronic (P123) dissolved into 76.04 mL of ethanol (97%) and was added to the above solution and stirred for 30 min. Second, an Ammonia solution was added to adjust the pH to ~8. The white precipitate was washed five times with distilled water and ethanol, dried for 24 h at 100 °C, and then annealed for 3 h at 450 °C.

3.2.2. Synthesis of (1, 3, 5 and 7% WO_3)/ TiO_2 Nanocomposite

A calculated amount of tungsten precursor (tungsten (VI) chloride) was dissolved in ethanol and then added to the titanium isopropoxide solution to produce a (1, 3, 5, and 7% WO_3)/ TiO_2 weight ratio. After that, the pH was adjusted using an ammonia solution, followed by washing and drying at 100 °C, and it was finally annealed for 3 h at 450 °C.

3.2.3. Synthesis of 4%Ag/ $x\%\text{WO}_3/\text{TiO}_2$

To prepare a 4% Ag-doped nanocomposite, the previously synthesized (1,3,5, and 7% WO_3)/ TiO_2 samples were suspended in a solution containing 0.063 g AgNO_3 and exposed to UV irradiation for 24 h to produce 4% Ag (1, 3, 5, and 7% WO_3)/ TiO_2 . Finally, the samples were dried at 60 °C for 24 h.

3.3. Characterization Techniques

The crystal structure of the prepared samples was evaluated using an X-ray diffractometer (XRD-6000, Shimadzu, Kyoto, Japan) with Cu K α radiation ($\lambda = 1.5406 \text{ \AA}$) operated at 40 kV and 30 mA. The synthesized nanoparticles' photoluminescence (PL) spectra were examined using a spectrofluorophotometer (RF-5301 PC, SHIMADZU, Kyoto, Japan) operating at room temperature with an excitation wavelength of 380 nm. Optical characteristics and optical bandgaps were determined using a diffused reflectance spectrometer (DRS UV-3600, SHIMADZU, Kyoto, Japan). The surface morphology analysis of pure TiO₂ and the 4%Ag/ x %WO₃/TiO₂ nanocomposite was performed using transmission electron microscopy (TEM JEM-2100F, Tokyo, Japan) that was employed to investigate particle sizes, shapes, and crystal planes. N₂ adsorption-desorption isotherms were employed to determine the specific surface area of the samples using a NOVA2000e apparatus (Quantachrome, Boynton Beach, FL, USA). Additionally, the photocatalytic activity of the prepared samples was illustrated via the photoreduction of Cr(VI) to Cr(III) using visible light irradiation (halogen lamp 1000 W, $\lambda > 420 \text{ nm}$) set at a 20 cm distance above the reactor. In detail, 50 mg of catalyst was added into 50 mL of Cr(VI) solution (10 mg L⁻¹) and suspended and maintained at a constant pH of 3.0 using 100 μ of formic acid as a hole scavenger. The mixture was placed in darkness to reach equilibrium. After that, it was illuminated with visible light, and 2 mL of each interval was centrifuged to remove suspended solids. The aqueous solution of the Cr(VI) sample was determined at $\lambda = 540 \text{ nm}$ using the diphenylcarbazide (0.5%) (DPC) solution in acetone and 0.2 M of H₂SO₄ that formed a violet color with Cr(VI) [56]. In addition, the catalytic activity for Cr(VI) reduction was evaluated using the formula (photocatalytic degradation = $(1 - C_t)/C_0$), where C_0 represents the initial concentration after the equilibrium experiment in the dark and C_t is the Cr(VI) concentration after the photoreduction process. Moreover, the photooxidation performance of the prepared materials was evaluated using MB dye as a module of the organic waste for the textile industrial sector. The oxidation efficiency was determined by withdrawing 2 mL of illuminated dye at each interval time and measuring the decreasing absorbance intensity of the dye using a spectrophotometer at $\lambda = 664 \text{ nm}$ using the same Cr(VI) degradation equation.

4. Conclusions

In our study, the synthesis of Ag/WO₃/TiO₂ nanocomposites with different concentrations of WO₃ particles via the sol-gel technique exhibited highly efficient photoactivity toward the two mechanisms of the photocatalyst performance. They show a good photoreduction of Cr(VI) ions that are converted to Cr(III) due to the impact of the plasmon effect of Ag. In addition, they exhibit a prerogative efficiency for the photo-oxidation of MB dye to CO₂ and H₂O.

Supplementary Materials: The following supporting information can be downloaded at: <https://www.mdpi.com/article/10.3390/catal14090633/s1>, Table S1 a comparative data for the current and the previous reported values of degradation rate of various related materials.

Author Contributions: Conceptualization, methodology, investigation, and writing—original/initial draft preparation, S.H.A.; formal analysis, review and editing, A.H.; formal analysis, original draft and supervision, M.S.; methodology, M.A.S.; conceptualization, formal analysis, review and editing, and supervision, A.M.A. All authors have read and agreed to the published version of the manuscript.

Funding: This research was funded by the Deanship of Research and Graduate Studies at King Khalid University, Saudi Arabia, grant number [RGP2/241/45].

Data Availability Statement: The data presented in this study are available on request from the corresponding author. The data are not publicly available due to it is a part of ongoing research for Ph.D. student.

Acknowledgments: The authors extend their appreciation to the Deanship of Research and Graduate Studies at King Khalid University for funding this work through the Large Research Project under grant number RGP2/241/45.

Conflicts of Interest: The authors declare no conflicts of interest.

References

- Lai, C.W. WO₃-TiO₂ Nanocomposite and Its Applications: A Review. *Nano Hybrids Compos.* **2018**, *20*, 1–26. [\[CrossRef\]](#)
- Khan, A.; Gaikwad, M.A.; Kim, J.H.; Kadam, A. An Overview and Experimental analysis of WO₃/TiO₂ Composite with Enhanced Electrochromic Properties for Smart Windows Application. *Tungsten* **2024**, *6*, 732–747. [\[CrossRef\]](#)
- Folli, A.; Bloh, J.Z.; Strøm, M.; Pilegaard Madsen, T.; Henriksen, T.; Macphee, D.E. Efficiency of Solar-Light-Driven TiO₂ Photocatalysis at Different Latitudes and Seasons. Where and When Does TiO₂ Really Work? *J. Phys. Chem. Lett.* **2014**, *5*, 830–832. [\[CrossRef\]](#) [\[PubMed\]](#)
- Kathirvelan, J.; Vijayaraghavan, R.; Thomas, A. Ethylene Detection Using TiO₂-WO₃ Composite Sensor for Fruit Ripening Applications. *Sens. Rev.* **2017**, *37*, 147–154. [\[CrossRef\]](#)
- Serga, V.; Burve, R.; Krumina, A.; Pankratova, V.; Popov, A.I.; Pankratov, V. Study of Phase Composition, Photocatalytic Activity, and Photoluminescence of TiO₂ with Eu Additive Produced by the Extraction-Pyrolytic Method. *J. Mater. Res. Technol.* **2021**, *13*, 2350–2360. [\[CrossRef\]](#)
- Matějová, L.; Kočí, K.; Reli, M.; Čapek, L.; Hospodková, A.; Peikertová, P.; Matěj, Z.; Obalová, L.; Wach, A.; Kuśtrowski, P.; et al. Preparation, Characterization and Photocatalytic Properties of Cerium Doped TiO₂: On the Effect of Ce Loading on the Photocatalytic Reduction of Carbon Dioxide. *Appl. Catal. B Environ.* **2014**, *152–153*, 172–183. [\[CrossRef\]](#)
- Li, T.; Luo, S.; Luo, Y.; Yang, L. Ag/AgI Nanoparticles Decorated WO₃/TiO₂ Nanotubes with Enhanced Visible Light Photocatalytic Activity. *Mater. Lett.* **2016**, *180*, 130–134. [\[CrossRef\]](#)
- Hirakawa, T.; Kamat, P. V Photoinduced Electron Storage and Surface Plasmon Modulation in Ag@TiO₂ Clusters. *Langmuir* **2004**, *20*, 5645–5647. [\[CrossRef\]](#)
- Jakob, M.; Levanon, H.; Kamat, P. V Charge Distribution between UV-Irradiated TiO₂ and Gold Nanoparticles: Determination of Shift in the Fermi Level. *Nano Lett.* **2003**, *3*, 353–358. [\[CrossRef\]](#)
- Wang, N.; Xu, Y.; Zhu, L.; Shen, X.; Tang, H. Reconsideration to the Deactivation of TiO₂ Catalyst during Simultaneous Photocatalytic Reduction of Cr (VI) and Oxidation of Salicylic Acid. *J. Photochem. Photobiol. A Chem.* **2009**, *201*, 121–127. [\[CrossRef\]](#)
- Vinodgopal, K.; Bedja, I.; Kamat, P. V Nanostructured Semiconductor Films for Photocatalysis. Photoelectrochemical Behavior of SnO₂/TiO₂ Composite Systems and Its Role in Photocatalytic Degradation of a Textile Azo Dye. *Chem. Mater.* **1996**, *8*, 2180–2187. [\[CrossRef\]](#)
- He, Y.; Wu, Z.; Fu, L.; Li, C.; Miao, Y.; Cao, L.; Fan, H.; Zou, B. Photochromism and Size Effect of WO₃ and WO₃-TiO₂ Aqueous Sol. *Chem. Mater.* **2003**, *15*, 4039–4045. [\[CrossRef\]](#)
- Archana, P.S.; Gupta, A.; Yusoff, M.M.; Jose, R. Tungsten Doped Titanium Dioxide Nanowires for High Efficiency Dye-Sensitized Solar Cells. *Phys. Chem. Chem. Phys.* **2014**, *16*, 7448–7454. [\[CrossRef\]](#)
- Yu, X.-F.; Wu, N.-Z.; Huang, H.-Z.; Xie, Y.-C.; Tang, Y.-Q. A Study on the Monolayer Dispersion of Tungsten Oxide on Anatase. *J. Mater. Chem.* **2001**, *11*, 3337–3342. [\[CrossRef\]](#)
- Pan, J.H.; Lee, W.I. Preparation of Highly Ordered Cubic Mesoporous WO₃/TiO₂ Films and Their Photocatalytic Properties. *Chem. Mater.* **2006**, *18*, 847–853. [\[CrossRef\]](#)
- Reyes-Gil, K.R.; Robinson, D.B. WO₃-Enhanced TiO₂ Nanotube Photoanodes for Solar Water Splitting with Simultaneous Wastewater Treatment. *ACS Appl. Mater. Interfaces* **2013**, *5*, 12400–12410. [\[CrossRef\]](#)
- Reyes-Gil, K.R.; Stephens, Z.D.; Stavila, V.; Robinson, D.B. Composite WO₃/TiO₂ Nanostructures for High Electrochromic Activity. *ACS Appl. Mater. Interfaces* **2015**, *7*, 2202–2213. [\[CrossRef\]](#)
- Vidyadharan, B.; Archana, P.S.; Ismail, J.; Yusoff, M.M.; Jose, R. Improved Supercapacitive Charge Storage in Electrospun Niobium Doped Titania Nanowires. *RSC Adv.* **2015**, *5*, 50087–50097. [\[CrossRef\]](#)
- Krishnan, S.G.; Archana, P.S.; Vidyadharan, B.; Misonon, I.I.; Vijayan, B.L.; Nair, V.M.; Gupta, A.; Jose, R. Modification of Capacitive Charge Storage of TiO₂ with Nickel Doping. *J. Alloys Compd.* **2016**, *684*, 328–334. [\[CrossRef\]](#)
- Chen, D.; Cheng, Y.; Zhou, N.; Chen, P.; Wang, Y.; Li, K.; Huo, S.; Cheng, P.; Peng, P.; Zhang, R. Photocatalytic Degradation of Organic Pollutants Using TiO₂-Based Photocatalysts: A Review. *J. Clean. Prod.* **2020**, *268*, 121725. [\[CrossRef\]](#)
- Chen, D.; Li, T.; Chen, Q.; Gao, J.; Fan, B.; Li, J.; Li, X.; Zhang, R.; Sun, J.; Gao, L. Hierarchically Plasmonic Photocatalysts of Ag/AgCl Nanocrystals Coupled with Single-Crystalline WO₃ Nanoplates. *Nanoscale* **2012**, *4*, 5431–5439. [\[CrossRef\]](#) [\[PubMed\]](#)
- Li, Y.; Wu, W.; Dai, P.; Zhang, L.; Sun, Z.; Li, G.; Wu, M.; Chen, X.; Chen, C. WO₃ and Ag Nanoparticle Co-Sensitized TiO₂ Nanowires: Preparation and the Enhancement of Photocatalytic Activity. *RSC Adv.* **2014**, *4*, 23831–23837. [\[CrossRef\]](#)
- Xu, J.Y.; Wen, C.; Jia, L.M.; Xiao, C.F. Ag/WO₃-Codoped TiO₂ Nanoparticles: Relation between Structure, Sorption, and Photocatalytic Activity. In Proceedings of the Second International Conference on Smart Materials and Nanotechnology in Engineering, Weihai, China, 8–11 July 2009; Volume 7493, pp. 1522–1528.
- Basumatary, B.; Basumatary, R.; Ramchiary, A.; Konwar, D. Evaluation of Ag@TiO₂/WO₃ Heterojunction Photocatalyst for Enhanced Photocatalytic Activity towards Methylene Blue Degradation. *Chemosphere* **2022**, *286*, 131848. [\[CrossRef\]](#) [\[PubMed\]](#)

25. Mineo, G.; Bruno, E.; Mirabella, S. Advances in WO₃-Based Supercapacitors: State-of-the-Art Research and Future Perspectives. *Nanomaterials* **2023**, *13*, 1418. [\[CrossRef\]](#)
26. Samuel, O.; Othman, M.H.D.; Kamaludin, R.; Sinsamphanh, O.; Abdullah, H.; Puteh, M.H.; Kurniawan, T.A. WO₃-Based Photocatalysts: A Review on Synthesis, Performance Enhancement and Photocatalytic Memory for Environmental Applications. *Ceram. Int.* **2022**, *48*, 5845–5875. [\[CrossRef\]](#)
27. Bahadur, J.; Agrawal, S.; Parveen, A.; Jawad, A.; Ashraf, S.S.Z.; Ghalib, R.M. Micro-Structural, Optical and Dielectric Properties of Ag Doped TiO₂ Synthesized by Sol–Gel Method. *Mater. Focus* **2015**, *4*, 134–141. [\[CrossRef\]](#)
28. Abdul Gafoor, A.K.; Musthafa, M.M.; Pradyumnan, P.P. AC Conductivity and Diffuse Reflectance Studies of Ag-TiO₂ Nanoparticles. *J. Electron. Mater.* **2012**, *41*, 2387–2392. [\[CrossRef\]](#)
29. Liu, S.; Guo, E.; Yin, L. Tailored Visible-Light Driven Anatase TiO₂ Photocatalysts Based on Controllable Metal Ion Doping and Ordered Mesoporous Structure. *J. Mater. Chem.* **2012**, *22*, 5031. [\[CrossRef\]](#)
30. Ismail, A.A.; Abdelfattah, I.; Helal, A.; Al-Sayari, S.A.; Robben, L.; Bahnemann, D.W. Ease Synthesis of Mesoporous WO₃-TiO₂ Nanocomposites with Enhanced Photocatalytic Performance for Photodegradation of Herbicide Imazapyr under Visible Light and UV Illumination. *J. Hazard. Mater.* **2016**, *307*, 43–54. [\[CrossRef\]](#)
31. Wahba, M.A.; Yakout, S.M.; Sheta, S.M.; Helal, A.; El-Sheikh, S.M. Robust Ferromagnetic V_{0.05-x}Co_xZn_{0.95}O (x = 0.01, 0.02, 0.03, 0.04, 0.05) Nano-Compounds: New Dilute Magnetic-Semiconductors with Tailored Optical Activity. *J. Alloys Compd.* **2024**, *1003*, 175503. [\[CrossRef\]](#)
32. Ernawati, L.; Wahyuono, R.A.; Muhammad, A.A.; Nurislam Sutanto, A.R.; Maharsih, I.K.; Widiastuti, N.; Widiyandari, H. Mesoporous WO₃/TiO₂ Nanocomposites Photocatalyst for Rapid Degradation of Methylene Blue in Aqueous Medium. *Int. J. Eng.* **2019**, *32*, 1345–1352. [\[CrossRef\]](#)
33. Araújo, E.S.; Leão, V.N.S. TiO₂/WO₃ Heterogeneous Structures Prepared by Electrospinning and Sintering Steps: Characterization and Analysis of the Impedance Variation to Humidity. *J. Adv. Ceram.* **2019**, *8*, 238–246. [\[CrossRef\]](#)
34. Sathasivam, S.; Bhachu, D.S.; Lu, Y.; Chadwick, N.; Althabaiti, S.A.; Alyoubi, A.O.; Basahel, S.N.; Carmalt, C.J.; Parkin, I.P. Tungsten Doped TiO₂ with Enhanced Photocatalytic and Optoelectrical Properties via Aerosol Assisted Chemical Vapor Deposition. *Sci. Rep.* **2015**, *5*, 10952. [\[CrossRef\]](#) [\[PubMed\]](#)
35. Ren, R.; Wen, Z.; Cui, S.; Hou, Y.; Guo, X.; Chen, J. Controllable Synthesis and Tunable Photocatalytic Properties of Ti³⁺-Doped TiO₂. *Sci. Rep.* **2015**, *5*, 10714. [\[CrossRef\]](#) [\[PubMed\]](#)
36. Gao, J.; Yang, W.; Fang, C.; Liang, J.; Cheng, T.; Li, P.; Guo, X.; Jung, Y.; Wang, Y.; Dong, X. Facile Synthesis of TiO₂/WO₃ Nanocomposites and the Electrochemical Lithiation/Delithiation Activity. *J. Mater. Sci.* **2021**, *56*, 14505–14517. [\[CrossRef\]](#)
37. Ramírez-Ortega, D.; Guerrero-Araque, D.; Acevedo-Peña, P.; Lartundo-Rojas, L.; Zanella, R. Effect of Pd and Cu Co-Catalyst on the Charge Carrier Trapping, Recombination and Transfer during Photocatalytic Hydrogen Evolution over WO₃-TiO₂ Heterojunction. *J. Mater. Sci.* **2020**, *55*, 16641–16658. [\[CrossRef\]](#)
38. Fang, H.; Cao, X.; Yu, J.; Lv, X.; Yang, N.; Wang, T.; Jiang, W. Preparation of the All-Solid-State Z-Scheme WO₃/Ag/AgCl Film on Glass Accelerating the Photodegradation of Pollutants under Visible Light. *J. Mater. Sci.* **2019**, *54*, 286–301. [\[CrossRef\]](#)
39. Roumaih, K.; Ismail, S.M.; Labib, S.; Helal, A. Structural, Magnetic, and Optical Properties of ZnFe₂O₄/RO (RO = CdO, NiO, Ga₂O₃, SnO₂, and TiO₂) Nanocomposites. *J. Mater. Sci.* **2023**, *58*, 7948–7967. [\[CrossRef\]](#)
40. Li, Y.; Chen, L.; Guo, Y.; Sun, X.; Wei, Y. Preparation and Characterization of WO₃/TiO₂ Hollow Microsphere Composites with Catalytic Activity in Dark. *Chem. Eng. J.* **2012**, *181*, 734–739. [\[CrossRef\]](#)
41. Sajjad, A.K.L.; Shamaila, S.; Tian, B.; Chen, F.; Zhang, J. One Step Activation of WO_x/TiO₂ Nanocomposites with Enhanced Photocatalytic Activity. *Appl. Catal. B Environ.* **2009**, *91*, 397–405. [\[CrossRef\]](#)
42. Bai, S.; Liu, H.; Sun, J.; Tian, Y.; Chen, S.; Song, J.; Luo, R.; Li, D.; Chen, A.; Liu, C.-C. Improvement of TiO₂ Photocatalytic Properties under Visible Light by WO₃/TiO₂ and MoO₃/TiO₂ Composites. *Appl. Surf. Sci.* **2015**, *338*, 61–68. [\[CrossRef\]](#)
43. Tryba, B.; Piszcz, M.; Morawski, A.W. Photocatalytic Activity of TiO₂-WO₃ Composites. *Int. J. Photoenergy* **2009**, *2009*, 1–7. [\[CrossRef\]](#)
44. Kubelka, P.; Munk, F. A Contribution to the Optics of Pigments. *Z. Technol. Phys.* **1931**, *12*, 593–599.
45. Tauc, J.; Grigorovici, R.; Vancu, A. Optical Properties and Electronic Structure of Amorphous Germanium. *Phys. Status Solidi B* **1966**, *15*, 627–637. [\[CrossRef\]](#)
46. Zhang, L.; Li, Y.; Zhang, Q.; Wang, H. Hierarchical Nanostructure of WO₃ Nanorods on TiO₂ Nanofibers and the Enhanced Visible Light Photocatalytic Activity for Degradation of Organic Pollutants. *CrystEngComm* **2013**, *15*, 5986. [\[CrossRef\]](#)
47. Ha, J.-H.; Muralidharan, P.; Kim, D.K. Hydrothermal Synthesis and Characterization of Self-Assembled h-WO₃ Nanowires/Nanorods Using EDTA Salts. *J. Alloys Compd.* **2009**, *475*, 446–451. [\[CrossRef\]](#)
48. de Castro, I.A.; Avansi, W.; Ribeiro, C. WO₃/TiO₂ Heterostructures Tailored by the Oriented Attachment Mechanism: Insights from Their Photocatalytic Properties. *CrystEngComm* **2014**, *16*, 1514–1524. [\[CrossRef\]](#)
49. Helal, A.; Yu, J.; Ghanem, M.A.; Labib, A.A.; El-Sheikh, S.M. Boosting the Photocatalytic Activity of Bismuth Vanadate (BiVO₄) via Optimization of the Internal Polarization. *J. Mol. Struct.* **2024**, *1312*, 138553. [\[CrossRef\]](#)
50. Lai, C.W.; Sreekantan, S. Incorporation of WO₃ Species into TiO₂ Nanotubes via Wet Impregnation and Their Water-Splitting Performance. *Electrochim. Acta* **2013**, *87*, 294–302. [\[CrossRef\]](#)
51. Khan, S.B.; Hou, M.; Shuang, S.; Zhang, Z. Morphological Influence of TiO₂ Nanostructures (Nanozigzag, Nanohelics and Nanorod) on Photocatalytic Degradation of Organic Dyes. *Appl. Surf. Sci.* **2017**, *400*, 184–193. [\[CrossRef\]](#)

52. Mohamed, M.M.; Ghanem, M.A.; Khairy, M.; Naguib, E.; Alotaibi, N.H. Zinc Oxide Incorporated Carbon Nanotubes or Graphene Oxide Nanohybrids for Enhanced Sonophotocatalytic Degradation of Methylene Blue Dye. *Appl. Surf. Sci.* **2019**, *487*, 539–549. [[CrossRef](#)]
53. Widiyandari, H.; Nashir, M.; Parasdila, H.; Almas, K.F.; Suryana, R. Ag-TiO₂ for Efficient Methylene Blue Photodegradation Under Visible Light Irradiation. *Bull. Chem. React. Eng. Catal.* **2023**, *18*, 593–603. [[CrossRef](#)]
54. Dong, P.; Yang, B.; Liu, C.; Xu, F.; Xi, X.; Hou, G.; Shao, R. Highly Enhanced Photocatalytic Activity of WO₃ Thin Films Loaded with Pt-Ag Bimetallic Alloy Nanoparticles. *RSC Adv.* **2017**, *7*, 947–956. [[CrossRef](#)]
55. Liu, Q.; Zhou, B.; Xu, M.; Mao, G. Integration of Nanosized ZIF-8 Particles onto Mesoporous TiO₂ Nanobeads for Enhanced Photocatalytic Activity. *RSC Adv.* **2017**, *7*, 8004–8010. [[CrossRef](#)]
56. Helal, A.; Salem, A.M.S.; El-Hout, S.I. Highly Efficient Visible Light Photoreduction of Cr(VI) via PANI/Bi₂S₃ Z-Scheme Behavior. *J. Photochem. Photobiol. A Chem.* **2024**, *447*, 115232. [[CrossRef](#)]

Disclaimer/Publisher's Note: The statements, opinions and data contained in all publications are solely those of the individual author(s) and contributor(s) and not of MDPI and/or the editor(s). MDPI and/or the editor(s) disclaim responsibility for any injury to people or property resulting from any ideas, methods, instructions or products referred to in the content.